

**Supplementary Information**

**Surface Distortion as a Unifying Concept and  
Descriptor in Oxygen Reduction Reaction  
Electrocatalysis**

*Raphaël Chattot<sup>1, 2, \*</sup>, Olivier Le Bacq<sup>3</sup>, Vera Beermann<sup>4</sup>, Stefanie Kühl<sup>4</sup>, Juan Herranz<sup>5</sup>,  
Sebastian Henning<sup>5</sup>, Laura Kühn<sup>6</sup>, Tristan Asset<sup>1</sup>, Laure Guétaz<sup>7</sup>, Gilles Renou<sup>3</sup>, Jakub  
Drnec<sup>2</sup>, Pierre Bordet<sup>8</sup>, Alain Pasturel<sup>3</sup>, Alexander Eychmüller<sup>6</sup>, Thomas J. Schmidt<sup>5, 9</sup>,  
Peter Strasser<sup>4</sup>, Laetitia Dubau<sup>1</sup> and Frédéric Maillard<sup>1, \*</sup>*

<sup>1</sup> Univ. Grenoble Alpes, CNRS, Grenoble INP<sup>⊥</sup>, Univ. Savoie Mont Blanc, LEPMI, 38000 Grenoble, France

<sup>2</sup> ESRF-The European Synchrotron, ID 31 Beamline, 38043 Grenoble, France

<sup>3</sup> Univ. Grenoble Alpes, CNRS, Grenoble INP<sup>⊥</sup>, SIMAP, 38000 Grenoble, France

<sup>4</sup> Electrochemical Energy, Catalysis and Material Science Laboratory, Department of Chemistry, Technische Universität Berlin, 10623 Berlin, Germany

<sup>5</sup> Electrochemistry Laboratory, Paul Scherrer Institut, 5232 Villigen, Switzerland

<sup>6</sup> Physical Chemistry, Technische Universität Dresden, 01062 Dresden, Germany

<sup>7</sup> CEA, LITEN, LCPEM, 38054 Grenoble, France

<sup>8</sup> CNRS, Institut Néel, F-38000 Grenoble, France

<sup>9</sup> Laboratory of Physical Chemistry, ETH Zurich, 8093 Zurich, Switzerland

\*e-mail: (RC) [raphael.chattot@grenoble-inp.org](mailto:raphael.chattot@grenoble-inp.org); (FM) [frederic.maillard@lepmi.grenoble-inp.fr](mailto:frederic.maillard@lepmi.grenoble-inp.fr)

<sup>⊥</sup> Institute of Engineering Univ. Grenoble Alpes

**This Supplementary Information file includes:**

Experimental Details

Supplementary Equations S1 to S16

Supplementary Figures S1 to S11

Supplementary Table S1 to S6

References

## Experimental details

### Reference Electrocatalyst

A Pt/Vulcan XC72<sup>®</sup> catalyst with a Pt weight fraction (wt. %) of 20% (TEC10V20E) was purchased from Tanaka Kikinzoku Kogyo (TKK) and used as reference material without any treatment.

### Synthesis of Partially-Aggregated Solid Pt/C Nanoparticles (A-Pt/C)

Partially-aggregated pure Pt/C nanoparticles were prepared *via* an aqueous synthesis protocol using monosodium citrate as a surfactant and sodium borohydride as a reducing agent. 7.92 mL of an aqueous Pt(IV) stock solution and 118 mg of monosodium citrate ( $\geq 99\%$ , Roth) were dissolved and stirred in a beaker containing 83 mL of deionized water. Then 12.5 mL of an aqueous solution of sodium borohydride (Aldrich 99.99 %, 204 mg of NaBH<sub>4</sub> powder in 50 mL of water) were added in a dropwise manner in 150 s. After the solution turned into a black slurry, the pH was then adjusted to 3 using a 0.5 M H<sub>2</sub>SO<sub>4</sub> (Suprapur<sup>®</sup> 96 %, Merck) aqueous solution and left for 24 extra hours. Finally, the solution was filtered and the filtrate copiously washed with deionized water before being dried at  $T = 110\text{ }^{\circ}\text{C}$  for 1 hour.

### Synthesis of Partially-Aggregated Solid PtNi/C Nanoparticles (A-PtNi/C)

To synthesize partially-aggregated solid PtNi/C nanoparticles, 53 mg of H<sub>2</sub>PtCl<sub>6</sub>·6H<sub>2</sub>O (99.9 % metals basis, Alfa Aesar) and 4.3 mg of NiCl<sub>2</sub>·6H<sub>2</sub>O metal salts (Putratronic<sup>®</sup> 99.9995 %, Alfa Aesar) were dissolved in a vial containing a 20 mL mixture of deionized water and ethylene glycol (EG) (Rotipuran<sup>®</sup>  $\geq 99.9\%$ , Roth) (volume ratio 1:1). 79 mg of a high surface area carbon black (Vulcan XC72<sup>®</sup>, Cabot) were dispersed by sonication in a separated vial containing also 20 mL of 1:1 EG:water mixture targeting 20 wt. % Pt. Then, the contents of each vial were mixed in 20 mL of pure EG, leading to a 2:1 EG:water volume ratio. The pH of the obtained mixture was then adjusted to 10 using a 0.5 M NaOH (Suprapur<sup>®</sup> 99.99 %, Merck) solution (diluted in 1:1 EG:water mixture). The resulting suspension was kept under vigorous stirring for 1 hour under argon atmosphere before being refluxed at  $T = 160\text{ }^{\circ}\text{C}$  for 3 hours. The solution was then allowed to cool down to room temperature under open air atmosphere for 12 hours with continuous stirring<sup>1</sup>. The pH of the mixture was then adjusted to 3 using a 0.5 M H<sub>2</sub>SO<sub>4</sub> (Suprapur<sup>®</sup>

96 %, Merck) aqueous solution and left for 24 extra hours. Finally, the solution was filtered and the filtrate copiously washed with deionized water before being dried at  $T = 110\text{ }^{\circ}\text{C}$  for 1 hour.

### **Synthesis of Hollow PtNi/C Nanoparticles (Hollow PtNi/C)**

To synthesize carbon-supported hollow PtNi/C nanoparticles, 154 mg of  $\text{Pt}(\text{NH}_3)_4\text{Cl}_2$  (Alfa Aesar, Specpure) and 180 mg of  $\text{NiCl}_2$  (Fluka, > 98.0 %) were first mixed with 300 mg Vulcan XC72<sup>®</sup> (Cabot), 10 mL of ethanol and 140 mL of de-ionized water (Millipore). An aqueous solution of  $\text{NaBH}_4$  (Aldrich 99.99 % - 5.5 mmol, 0.22 M) was then added at a rate of  $5\text{ mL min}^{-1}$  and stirred for 1 hour under magnetic stirring at room temperature ( $T = 25\text{ }^{\circ}\text{C}$ ). The resulting mixture was filtered, thoroughly washed by de-ionized water and dried for 45 minutes at  $T = 110\text{ }^{\circ}\text{C}$ . The catalysts powder was then acid-treated for  $t = 22$  hours in a stirred 1 M  $\text{H}_2\text{SO}_4$  (Suprapur<sup>®</sup> 96 %, Merck) solution at  $T = 20\text{ }^{\circ}\text{C}$  and then filtered, washed and dried again following the same procedure.

### **Synthesis of Aerogel PtNi (Aerogel PtNi)**

Unsupported PtNi aerogel was synthesized according to the protocol presented in Ref. <sup>2</sup>. Briefly, 585  $\mu\text{L}$  of a 0.205 M aqueous  $\text{H}_2\text{PtCl}_6$  solution (8 wt. %, Sigma Aldrich) and 4 mL of a 10 mM aqueous  $\text{NiCl}_2 \cdot 6\text{H}_2\text{O}$  solution (99% Sigma Aldrich) were dissolved and stirred in 790 mL water. Then, 7 mL of a 0.1 M  $\text{NaBH}_4$  solution (99.99%, Sigma-Aldrich) were added, and the solution was maintained under vigorous stirring 30 min after its colour changed from yellow to deep brown. The solution was then divided into 100 mL vials and left *ca.* four days under ambient conditions. The synthesis product was then collected by sequentially change half of the supernatant with fresh water (6 times) and acetone (11 times) and using a critical point dryer (Critical Point Dryer 13200J-ABn SPI Supplies) operating with  $\text{CO}_2$ .

### **Synthesis of Sponge PtNi/C Nanoparticles (Sponge PtNi/C)**

Sponge PtNi/C nanoparticles were synthesized via an ‘in-house’ polyol method. 120 mg of Vulcan XC72<sup>®</sup> (Cabot), 54 mg of  $\text{Pt}(\text{NH}_3)_4\text{Cl}_2$  (Premion<sup>®</sup> 99.995% metals basis, Alfa Aesar) and 37 mg  $\text{NiCl}_2 \cdot 6\text{H}_2\text{O}$  metal salts (99.9 % metals basis, Alfa Aesar) were mixed in 20 mL ethylene glycol. After setting the pH to 9-10 by dropwise addition of a 5 wt. % solution of KOH in EG (Rotipuran<sup>®</sup>  $\geq 99.9\text{ }%$ ,

Roth), the solution was heated in reflux at  $T = 200\text{ }^{\circ}\text{C}$  for 20 hours. The final product was allowed to cool in open atmosphere and was then collected by filtration and dried at  $T = 110\text{ }^{\circ}\text{C}$  for 45 minutes. The catalysts powder was then acid-treated for  $t = 22$  hours in a stirred 1 M  $\text{H}_2\text{SO}_4$  (Suprapur<sup>®</sup> 96 %, Merck) solution at  $T = 20\text{ }^{\circ}\text{C}$  and then filtered, washed and dried again following the same procedure.

### **Synthesis of PtNi/C Octahedra (Octahedron PtNi/C)**

To prepare PtNi/C octahedra, we used the method originally introduced by Zhang *et al.*<sup>3</sup>. Briefly,  $\text{Pt}(\text{acac})_2$  (160 mg, Alfa Aesar, Pt 48.0 % min) and  $\text{Ni}(\text{acac})_2$  (240 mg, Alfa Aesar, 95 %) salts precursors were dissolved in oleylamine (48 mL, Sigma-Aldrich,  $\geq 98\%$ ) and oleic acid (32 mL, Alfa Aesar, tech. 90%). The solution was then deaerated with  $\text{N}_2$  and heated at  $T = 60\text{ }^{\circ}\text{C}$  for 20 minutes. Afterwards, the solution was further heated to  $T = 130\text{ }^{\circ}\text{C}$  at a rate of  $\sim 5\text{ }^{\circ}\text{C}$  per minute and  $\text{W}(\text{CO})_6$  reducing agent powder (560 mg, Alfa Aesar, 97 %) was quickly introduced and  $\text{N}_2$  flow stopped. The solution was further heated to  $T = 230\text{ }^{\circ}\text{C}$  and stirred for 45 minutes. The as-produced octahedra were collected by centrifugation: after the solution has cooled down, 60 mL ethanol and 20 mL toluene (Roth,  $\geq 99.8\%$ ) were added to the solution which was further divided in 4 centrifugation tubes, and centrifuged at 8000 rpm for 15 minutes. The as-separated nanoparticles were re-dispersed in 20 mL toluene, while 160 mg of Vulcan XC-72R was ultrasonically dispersed in 20 mL toluene in a separated vial. The carbon support and nanoparticles were then mixed and dispersed with an ultrasonic horn for 30 minutes. The final product was finally centrifuged again (same conditions). To wash the carbon-supported nanoparticles the supernatant was replaced with ethanol and then centrifuged 3 consecutive times and finally freeze-dried.

### **Synthesis of PtNi/C Cube (Cube PtNi/C)**

To prepare PtNi/C cubes, we used the method originally introduced by Zhang *et al.*<sup>3</sup>. Briefly,  $\text{Pt}(\text{acac})_2$  (80 mg, Alfa Aesar, Pt 48.0 % min) salt precursor was dissolved in oleylamine (36 mL, Sigma-Aldrich,  $\geq 98\%$ ) and oleic acid (4 mL, Alfa Aesar, tech. 90%). The solution was then deaerated with  $\text{N}_2$  and heated at  $T = 80\text{ }^{\circ}\text{C}$  for 15 minutes. Afterwards the solution was further heated to  $T = 130\text{ }^{\circ}\text{C}$  and 200 mg of  $\text{W}(\text{CO})_6$  powder (Alfa Aesar, 97 %) was quickly introduced and the  $\text{N}_2$  flow stopped. The solution

was then heated from 130 °C to 200 °C, at a rate of  $\sim 4$  °C min<sup>-1</sup>. During the heating process, a dropwise addition (107  $\mu$ L min<sup>-1</sup>) from a stock solution of 238 mg NiCl<sub>2</sub>.6H<sub>2</sub>O (Alfa Aesar, 99.9 % metals basis) dissolved in 10 mL oleylamine (Sigma-Aldrich,  $\geq 98$ ) and 10 mL oleic acid (Alfa Aesar, tech. 90 %). The temperature was then further increased to  $T = 240$  °C and maintained during 15 minutes. The process to collect, support and wash the nanoparticles was the same that for the PtNi octahedra.

### **Synthesis of Pt/C Cube (Cube Pt/C)**

Cube Pt/C was obtained by the exact same protocol that for the PtNi octahedra, but without the addition of a Ni salt precursor.

### **Synthesis of Sphere PtNi/C (Sphere PtNi/C)**

Sphere PtNi/C were prepared using a protocol adapted from Gan *et al.*<sup>4</sup>, also referred at the ‘hot injection’ method. In brief, Ni(acac)<sub>2</sub> metal precursor (77 mg, Alfa Aesar, 95 %) and 92 mg of 1, 2-tetradecanediol (TDD) reducing agent (Sigma-Aldrich 90 %) were dissolved in dibenzylether (30 mL, Sigma-Aldrich,  $\geq 98.0$  %) in the presence of oleylamine (0.3 mL, Sigma-Aldrich,  $\geq 98$ ) and oleic acid (0.3 mL, Alfa Aesar, tech. 90%). After the solution was heated at  $T = 80$  °C under N<sub>2</sub> flow for 30 minutes, the temperature was further increased to  $T = 200$  °C. At this temperature, a solution of Pt(acac)<sub>2</sub> (40 mg, Alfa Aesar, Pt 48.0 %) in 1, 2-dichlorobenzene (1.4 mL, Alfa Aesar, 99 %) was quickly introduced in the reactor. The solution was kept under continuous stirring at  $T = 200$  °C for 1 hour. The process to collect, support and wash the nanoparticles was the same that for the PtNi octahedra.

### **Synchrotron Wide-Angle X-Ray Scattering (WAXS) Measurements**

Synchrotron WAXS measurements were performed at ID31 beamline of the European Synchrotron Radiation facility (ESRF) in Grenoble, France. The high energy X-ray radiation (61 keV or 0.20 Å) was focused on the catalyst powders contained in a 1 mm diameter Kapton<sup>®</sup> capillary, and the scattered signal was collected using a Dectris Pilatus CdTe 2M detector positioned 300 mm behind the sample. The size of the beam at the sample position was 4 × 30  $\mu$ m (vertical × horizontal). The energy, detector distance and tilts were calibrated using a standard CeO<sub>2</sub> powder and the 2D diffraction patterns were reduced to the presented 1D curves using the pyFAI software package<sup>5</sup>. For the electrochemically aged samples,

the aged catalyst thin films were collected from the glassy carbon electrode using a Kapton<sup>®</sup> tape and characterized in transmission mode.

### **Rietveld Refinements**

Rietveld refinement of the WAXS patterns was performed to extract the crystallite size, lattice parameter and microstrain <sup>6</sup> using the *Fm3m* structure of Pt metal and the Fullprof software. The instrumental resolution function was determined by the refinement of a CeO<sub>2</sub> standard sample. After several trials, the Thomson-Cox-Hastings profile function was adopted with possibility for uniaxial anisotropic broadening from size origin <sup>7</sup>. The background of patterns was described by an interpolated set of points with refinable intensities (this procedure allowed a more accurate description of the background leading to improved diffraction peak profiles).

### **Density Functional Theory (DFT) Calculations**

#### *Approach and computational details for estimation of chemical disorder*

DFT calculations were used to estimate the broadening of the X-ray diffraction patterns induced by chemical disorder. We used the work of E. Parzen <sup>8</sup>, which introduced a statistical analysis of the chemically-induced local deformations around each atom of a simulation cell. DFT calculations proved well-suited to determine the fine geometry around each atom and provided the accuracy necessary to estimate the contribution of chemical disorder to the values of microstrain. Since a single simulation cell can hardly represent all the possible structural arrangements of Pt and Ni atoms that can be found in a nanometre-sized alloy, large cells of 500 atoms were considered for simulating real-life nanomaterials. Moreover, estimator functions were used to transpose the (atomic-level) information provided by DFT calculations to the nanometre-scale probed by X-rays.

The DFT calculations were performed using the methodology described below. The simulation cells contained 500 Pt atoms and had face-centred cubic (fcc) structure. The Pt atoms were first substituted by Ni atoms until the desired Ni content was reached. Six cells in which the Ni content varied between 10 and 60 at. % were built. The DFT calculations were performed using the Vienna *ab initio* simulation package (VASP) code within the projector augmented wave (PAW) method <sup>9,10</sup>. The general gradient

approximation within the Perdew–Burke–Ernzerhof formulation <sup>11</sup> was found an adequate choice for the exchange and correlation functional. The Hellmann–Feynman theorem <sup>12,13</sup> was used to optimize the total volume of the cell and to relax the atomic positions after elemental substitution. The atomic coordinates were considered fully relaxed when the amplitude of the individual forces was less than 0.001 eV Å<sup>-1</sup>. Numerical integrations in the Brillouin zone were performed by means of the Hermite–Gaussian method <sup>14</sup>. A single  $k$ -point ( $\Gamma$  point) was found adequate for total energies of the 500-atom cells to be converged within 10<sup>-4</sup> eV with an energy cut-off of 260 eV.

#### *Chemical disorder-induced local deformations of the simulation cells*

Atomic-level deformations can be characterized by calculating the tensor of the gradient of deformation ( $F_k$ ) around a given atom ( $k$ ) whose components express the space-dependent distortions ( $f_{\alpha\beta} = (\Delta d/d_0)_{\alpha\beta}$ ) of the first-neighbour cage around  $k$  and  $\alpha$  and  $\beta$  indexes run over  $x$ ,  $y$  and  $z$  space variables. This operator was used to transform the relaxed atomic positions,  $x_i$ , into the atomic positions of the perfect fcc-structure,  $X_i$ , so that  $F_k X_i = x_i$ , where  $i$  runs over the 12 first neighbours of the  $k$  atom.

**Fig. S2.a** illustrates the theoretical approach used in this study.

For a given chemical composition (10 < Ni at. % < 60 %), the 12  $X_i$  coordinates were fixed by the fcc structure of the cell and the  $x_i$  by the relaxation of the atomic positions. The components of the  $F_k$  tensor were determined so that  $F_k X_i \rightarrow x_i$ , which was made possible by minimizing the sum:

$$\sum_{i=1}^{12} |F_k X_i - x_i| \quad \text{Eq. S1}$$

by means of a least-square algorithm. If the knowledge of the 9 components of the  $F_k$  tensor is the most complete and accurate description of the local deformation around a  $k$  atom, this information must be recast into a single numerical value to be directly comparable to the microstrain value estimated by refinement of the WAXS patterns.

To this goal, we used the approach introduced in the work of Stukowski *et al.* <sup>15</sup>. Briefly, the matrix of the gradients of deformation was rewritten in the local basis-set corresponding to the principal axis of deformation for which it adopted a diagonal form. The three eigenvalues represent the microstrain along



the three directions defined by the principal axis, the first one,  $\epsilon_1$ , corresponds to the larger strain met around the considered atom. Note that these principal axes were different from one site to another, given that the first principal axis corresponds to the largest local deformation around the central site, which obviously depends on the local chemistry. As no crystallographic direction had to be favoured, the local deformation around each  $k$  atom was finally written in a more symmetric expression by using:

$$\delta_k = \left( \frac{\epsilon_1^2 + \epsilon_2^2 + \epsilon_3^2}{3} \right)^{1/2} \quad \text{Eq. S2}$$

This descriptor is still a local parameter. A statistic over these parameters was undertaken to provide an average response representative of X-ray measurements.

#### *Average microstrain in the simulation cell*

For each cell, a density of atomic distortions was obtained from the data of the 500 individual atomic distortions,  $\delta_k$ , by performing a gaussian kernel estimation<sup>8</sup>. In this method, the non-parametric estimator used to approximate the density function reads:

$$\widehat{D}_h(\delta) = \frac{1}{Nh} \sum_{k=1}^N K\left(\frac{\delta - \delta_k}{h}\right) \quad \text{Eq. S3}$$

where  $K(x) = (2\pi)^{-1/2} \exp(-x^2/2)$ .  $K$  is the kernel function (here having a Gaussian shape) and  $h$  is the smoothing parameter. If the choice of the Kernel function generally affects the estimator, the value of  $h$  deeply influences the final shape of the distribution. A small  $h$  value generated contrived details in the estimator function. In contrast, a large  $h$  value led to an approximation of the primary features of the curve. Consequently, the choice of the parameter  $h$  was determinant, and a specific study was undertaken to fix its value. To this goal, we generated the estimator of the density of local deformations for a series of smoothing factors varying from 0.01 %% to 0.75 %% (0.01, 0.05, 0.1, 0.2, 0.30, 0.5 and 0.75 %%).

**Fig. S3** displays examples of the so-obtained densities in the cells containing 10 and 40 at. % Ni for selected values of the parameter  $h$ , namely 0.05, 0.2 and 0.75 %. Clearly, the density curve (black line) adopts a shape that better obeys a Gaussian law (dotted purple line) with increasing values of  $h$ . It is no surprise that a low Ni content leads to a more Gaussian shape compared to higher Ni contents

(**Figs. S3b** and **S3e**) since the number of possible arrangements of atoms in the cell is far less numerous in the first case. We must emphasize that, if the approximations due to the limited statistics could have been addressed by multiplying the number of cells with various Ni compositions, the huge amount of calculations that would be necessary was unfortunately unaffordable in terms of computational resources.

From that, our strategy consisted in estimating the microstrain from the Root Mean Square (RMS) deviation  $\sigma$  of the Gaussian distortion density distributions<sup>15</sup>. This microstrain, directly read from the value of  $\sigma$  are plotted in **Fig. S2.b** as a function of the Ni content and for the various values of  $h$  investigated. It is clear that very similar experimental trends and microstrain values were obtained whatever the value of  $h$  (and this for different Ni contents). These calculations provided an estimation of the error made on the calculation of the average microstrain, as shown in **Fig. 3** in the main text. It was supposed that the possible effect of temperature on the atomic rearrangement during the relatively low temperature catalysts synthesis and/or X-ray characterizations ( $T < 240^\circ\text{C}$ ) was comprised in this error. While a more precise estimation of such effects would be interesting, it is out of the scope of this paper.

#### *Catalytic site configuration heterogeneity in structurally-disordered materials*

To characterize the surface state of the nanomaterials in tight connection with their catalytic activity, Pt or PtNi 7-layer slabs (face-centred cubic structure, fcc) were built (**Fig. S6.a**). Since the most stable facet of nanometre-sized crystallites with fcc structure is (111), slabs were orientated along the (111) direction (hexagonal symmetry). Experimentally, atomic defects are generated at the surface of PtNi/C nanoparticles during post-synthesis acidic treatment or under PEMFC cathode operation. To reproduce these ageing processes, atomic vacancies were introduced at random in the slabs but with a higher concentration in the surface layers. An overall amount of 35 % of vacancies was chosen for this specific study. The influence of the density of vacancies on the reconstruction of the slab has been previously discussed in Ref.<sup>16</sup>. A slab (**Fig. S6.b**) was also built by substituting randomly 24 Pt atoms by Ni atoms in the three central layers of the previous slab, leading to a global Ni content of 12 at. % As the implementation of the vacancies was identical in both cells, our approach allowed a quantitative

estimation of the eventual influence of the presence of Ni atoms in the core layers on the chemisorption properties of structurally-disordered materials.

**Fig. S6.b** and **Fig. S6.e** present the deformation map in the surface: an average of the interatomic distances around each surface atom is calculated and compared to a reference distance, chosen to be 2.71 Å for both cells. Every surface atom having an average interatomic distance smaller/larger than the in-plane lattice parameter of the Ni-free slab is considered in a compression/expansion state, respectively. From these cartographies, it appears clearly that, if many types of deformed geometries exist on the surface of the nanocatalysts, the influence of the inner layers (containing or not Ni atoms) is weak. Let us insist on the fact that the same reference was kept for the calculation of the average deformation. The use of the in-plane lattice of the cell containing Ni (2.63 Å) as a reference for the calculation of the average deformation of this cell should lead to an expansion state for all the surface atoms (map only in the tone of red). Our representation (fixed reference) outlines the similarities of situation for the Pt surface atoms in both cells and suggests similar chemisorption properties.

In **Figs. S6.c** and **S6.f**, we adopted a new representation for the average deformation,  $\delta d$ , centred on each surface site, as a function of the coordination number (CN) of the sites. The colour of the point refers to the colour bar of **Figs. S6.b** and **S6.e**. It is striking to observe that, for a given CN, numerous deformation states exist. **Figs. S6.c** and **S6.f** show that, the reconstruction of the Pt surface in the presence of vacancies leads to a wide distribution of catalytic site configurations. The proportion of sites for each category of CN is similar for both slabs. Nevertheless, the geometry of the surface adopted by the slab containing Ni atoms tends to slightly increase the structural disorder as suggested by the broadening of the set points of average deformations for a given CN.

The OH\* adsorption energies relative to a non-defective Pt(111) site were calculated on selected sites of the slabs (labelled  $\alpha$  in the Pt slab and  $\beta$  in the PtNi slab) to get insights into their chemisorption properties<sup>17</sup>. The values presented in **Fig. S6.g** unambiguously show various affinity for OH adsorbates. The maximum amplitude of these variations (in the order of the eV) largely contains the ~0.1 eV energy decrease required to maximize the ORR activity<sup>18</sup>. These DFT calculations theoretically confirm that, unlike structurally-ordered catalysts with uniformly tailored surface, structurally-disordered catalysts

rest on a scattergun approach, where the proportion of active sites with nearly optimal binding energy to the ORR intermediates dominate the global reaction rate.

### **Atomic Absorption Spectroscopy Measurements**

Atomic Absorption Spectroscopy (AAS) was used to quantify the Pt weight fraction (wt. %) in the synthesized catalysts. The measurements were performed using a AAS-PinAACLE 900F from PerkinElmer. 5 mg of the electrocatalysts were first dissolved in aqua regia (HCl: HNO<sub>3</sub> 3:1 volume ratio) made from high purity acids (37 vol. % ACS Reagent, Sigma -Aldrich and 65 vol. % Sigma-Aldrich for HCl and HNO<sub>3</sub> respectively) for 72 hours at  $T = 25^{\circ}\text{C}$ . The solution was then diluted sevenfold to reach a range around 50-200 ppm Pt. The metal contents were then determined using three series of three measurements. The wavelength considered for Pt was  $\lambda = 240.7\text{ nm}$  and a 37 mm hollow cathode lamp (Heraeus) was used.

### **Electron Microscopy (STEM/X-EDS and HAADF-HRSTEM)**

The STEM/X-EDS elemental maps were acquired using a JEOL 2100F microscope operated at 200 kV equipped with a retractable large angle Silicon Drift Detector (SDD) Centurio detector. The X-EDS spectra were recorded on different magnifications, from hundreds to individual nanoparticles by scanning the beam in a square region of various sizes. The quantitative analyses were performed on Pt  $L$  and Ni  $K$  lines using the  $K$ -factors provided by the JEOL software. The HRSTEM images were acquired using a FEI-Titan Ultimate microscope. This microscope was equipped with two aberration correctors allowing a  $< 0.1\text{ nm}$  spatial resolution in STEM mode. If needed (better chemical contrast), images were collected on a High Angle Annular Dark Field (HAADF) detector.

### **Electrochemical Characterization**

All the glassware accessories used in this study were first cleaned by soaking in a H<sub>2</sub>SO<sub>4</sub>:H<sub>2</sub>O<sub>2</sub> mixture for at least 12 hours, thoroughly washing and then boiling in Milli-Q water (Millipore, 18.2 M $\Omega$  cm, total organic compounds  $< 3\text{ ppb}$ ). An Autolab PGSTAT302N potentiostat and a custom-made four-electrode electrochemical cell thermostated at  $T = 25^{\circ}\text{C}$  were used. The electrolyte (0.1 M HClO<sub>4</sub>) was daily prepared using Milli-Q water and HClO<sub>4</sub> 96 wt. % (Suprapur<sup>®</sup>, Merck). The counter-electrode was

a Pt grid and the reference electrode a commercial RHE (Hydroflex, Gaskatel GmbH) connected to the cell via a Luggin capillary. A Pt wire connected to the reference electrode was used to filter the high frequency electrical noise. To prepare the thin-film rotating disk working electrodes <sup>19</sup>, a suspension containing 10 mg of the targeted ~20 wt. % Pt(Ni) catalyst powder, 54  $\mu\text{L}$  of 5 wt. % Nafion<sup>®</sup> solution (Electrochem. Inc.), 1446  $\mu\text{L}$  of isopropanol and 3.6 mL (18.2 M $\Omega$  cm) of deionized water (MQ-grade, Millipore) was made. After sonication for 15 minutes, 10  $\mu\text{L}$  of the suspension was pipetted onto a 0.196 cm<sup>2</sup> glassy carbon disk under rotation at 700 rpm, and gently dried with a heat gun while the rotation was maintained (spin coating technique <sup>20</sup>) to ensure evaporation of the Nafion<sup>®</sup> solvents, yielding a loading of *ca.* 20  $\mu\text{g}_{\text{Pt}} \text{cm}^{-2}_{\text{geo}}$ . Prior to any electrochemical experiment, the working electrode was immersed into the deaerated electrolyte at  $E = 0.40 \text{ V vs. RHE}$  (Ar >99.999 %, Messer). The following electrochemical techniques were then sequentially performed:

Step 1: Impedance Electrochemical Spectroscopy (EIS) measurements ( $E = 0.4 \text{ V vs. RHE}$ ,  $\Delta E = 10 \text{ mV}$ , 20 frequencies between 20 Hz and 100 kHz) were performed to determine the Ohmic resistance of the cell. 90% of the resistance value was then dynamically compensated by the potentiostat software (Nova 2.1).

Step 2: the base cyclic voltammograms were recorded in Ar-saturated electrolyte between 0.05 V and 1.23 V vs. RHE with a potential sweep rate of 500 (50 potential cycles, activation step) or 20 mV s<sup>-1</sup> (3 potential cycles, base voltammograms).

Step 3: the Pt electrochemically active surface area (ECSA) was estimated using CO<sub>ads</sub> stripping coulometry. In brief, a monolayer of CO<sub>ads</sub> was formed on the electrocatalyst surface by bubbling CO gas (> 99.997 %, Messer) in the electrolyte for 6 min while keeping the electrode potential at  $E = 0.1 \text{ V vs. RHE}$ , purging with Ar for 34 min while remaining at the same potential, and finally stripping off (electrooxidizing) this CO<sub>ads</sub> layer by recording 3 cyclic voltammograms between 0.05 V and 1.23 V vs. RHE at 20 mV s<sup>-1</sup>. The electrical charge required to electrooxidize the CO<sub>ads</sub> monolayer provided the ECSA assuming a conversion factor of 420  $\mu\text{C}$  per cm<sup>2</sup> of Pt.

Step 4: the electrocatalytic activity for the ORR was measured in O<sub>2</sub>-saturated 0.1 M HClO<sub>4</sub> solution (20 minutes of purging by oxygen > 99.99 %, Messer, the electrode potential being maintained at  $E = 0.4$  V vs. RHE) using cyclic voltammetry between 0.20 and 1.05 V vs. RHE at a potential sweep rate of 5 mV s<sup>-1</sup> and at different rotational speeds in the order: 400 (2 consecutive measurements), 900, 1600, 2500 and 400 rpm again. The kinetic current for the ORR was calculated on the 1600 rpm positive-going potential scan after correction of Ohmic drop and O<sub>2</sub> diffusion in solution (Koutecky-Levich equation):

$$I_k = \frac{I * I_{lim}}{I_{lim} - I} \quad \text{Eq. S4}$$

Where  $I$  is the measured current,  $I_k$  is the kinetic current and  $I_{lim}$  is the diffusion-limited current

The ORR specific/mass activity was determined by normalizing the current measured at  $E = 0.95$  V vs. RHE from the 1600 rpm positive-going scan, after correction from the oxygen diffusion in solution and the Ohmic drop, to the real surface area/mass of deposited Pt determined by CO<sub>ads</sub> stripping voltammetry or AAS respectively.

### Accelerated Stress Tests

The accelerated stress tests were performed in a second electrochemical cell containing freshly-prepared 0.1 M HClO<sub>4</sub> electrolyte and thermostated at  $T = 80$  °C. The ‘durability’ cell was in all points similar to the ‘characterization’ cell, except that in order to avoid Pt dissolution at the counter electrode/Pt<sup>z+</sup> ions redeposition at the working electrode, the Pt grid was replaced by a glassy carbon plate. The potential of the working electrode was cycled between 0.6 and 1.0 V vs. RHE using a linear sweep ramp and a potential sweep rate of 50 mV s<sup>-1</sup>. Individual electrodes were used to investigate the effect of the number of potential cycles (2<sup>nd</sup> ORR, 100, 5,000 and 20,000 potential cycles). Consequently, each electrode was electrochemically characterized twice (before and after cycling), and only the number of potential cycles changed.

### Estimation of the ‘Surface Atoms Ratio’ $D$

This parameter is defined by Montejano-Carrizales *et al.* in their mathematical model of face-centred cubic cuboctahedral particles <sup>21,22</sup>:

$$D = 100 \frac{N_s}{N} \quad \text{Eq. S5}$$

And  $N$  and  $N_s$  are the total number of atoms and the number of surface atoms, respectively:

$$N = 10 \frac{m^3}{3} + 5m^2 + \frac{11}{3}m + 1 \quad \text{Eq. S6}$$

$$N_s = 10m^2 + 2 \quad \text{Eq. S7}$$

‘ $m$ ’ corresponds to the number of atomic layers composing the crystallite in the Montejano-Carrizales model. The values of ‘ $m$ ’ are linked to the crystallite size ‘ $d$ ’ size by the relation:

$$m = \frac{d}{2\sqrt{3}r_{\text{Pt}}} \quad \text{Eq. S8}$$

With ‘ $r_{\text{Pt}}$ ’ the covalent radius of a Pt atom ( $r_{\text{Pt}} = 0.135$  nm).

In this study,  $D$  is calculated for each catalyst based on its measured crystallite size  $d$  from WAXS.

The values of  $D$  are displayed **Table S2**.

### Extraction of the Surface Distortion (SD) descriptor

As discussed in the manuscript, the as-measured microstrain determined from Rietveld refinement of wide-angle X-ray scattering (WAXS) patterns is linked to the Surface Distortion (SD) by the following relation:

$$\text{Microstrain} = f(\% \text{Ni}) + \text{Surface Distorsion} * D \quad \text{Eq. S9}$$

For a set of catalysts composed of alloyed and monocrystalline nanoparticles (*i.e.* without surface distortion),  $\text{SD} = 0$  and **Eq. S9** can be simplified as:

$$\text{Microstrain} = f(\% \text{Ni}) \quad \text{Eq. S10}$$

As confirmed by DFT calculations and shown in **Fig. S4.a**, Pt/C TKK, Cube PtNi/C, Octahedron PtNi/C and Sphere PtNi/C satisfy the conditions of **Eq. S10**. Consequently,  $f$  was determined from a fit of these experimental data points (see **Fig. S4**).

As presented in **Fig. S4**, using a third order polynomial function instead of a linear one has two main advantages: (i) such a function can perfectly intercept a set of 4 data points without any error and (ii) it naturally features local extrema, suggesting the presence of a maximum Ni contribution to the microstrain value (reached for a Ni composition around 50 at. %), which makes physical sense. Indeed, one may expect this maximum when considering that in a solid solution the role of ‘foreign’ and ‘host’ elements reverse at the 50:50 at. % composition.

The polynomial fit in the region of the experimental data reads:

$$f(\%Ni) = \sum_{i=0}^3 \alpha_i (\%Ni)^i \quad \text{Eq. S11}$$

With:

$$\alpha_0 = 0 \quad \text{Eq. S12}$$

$$\alpha_1 = -1 \quad \text{Eq. S13}$$

$$\alpha_2 = 0.16 \quad \text{Eq. S14}$$

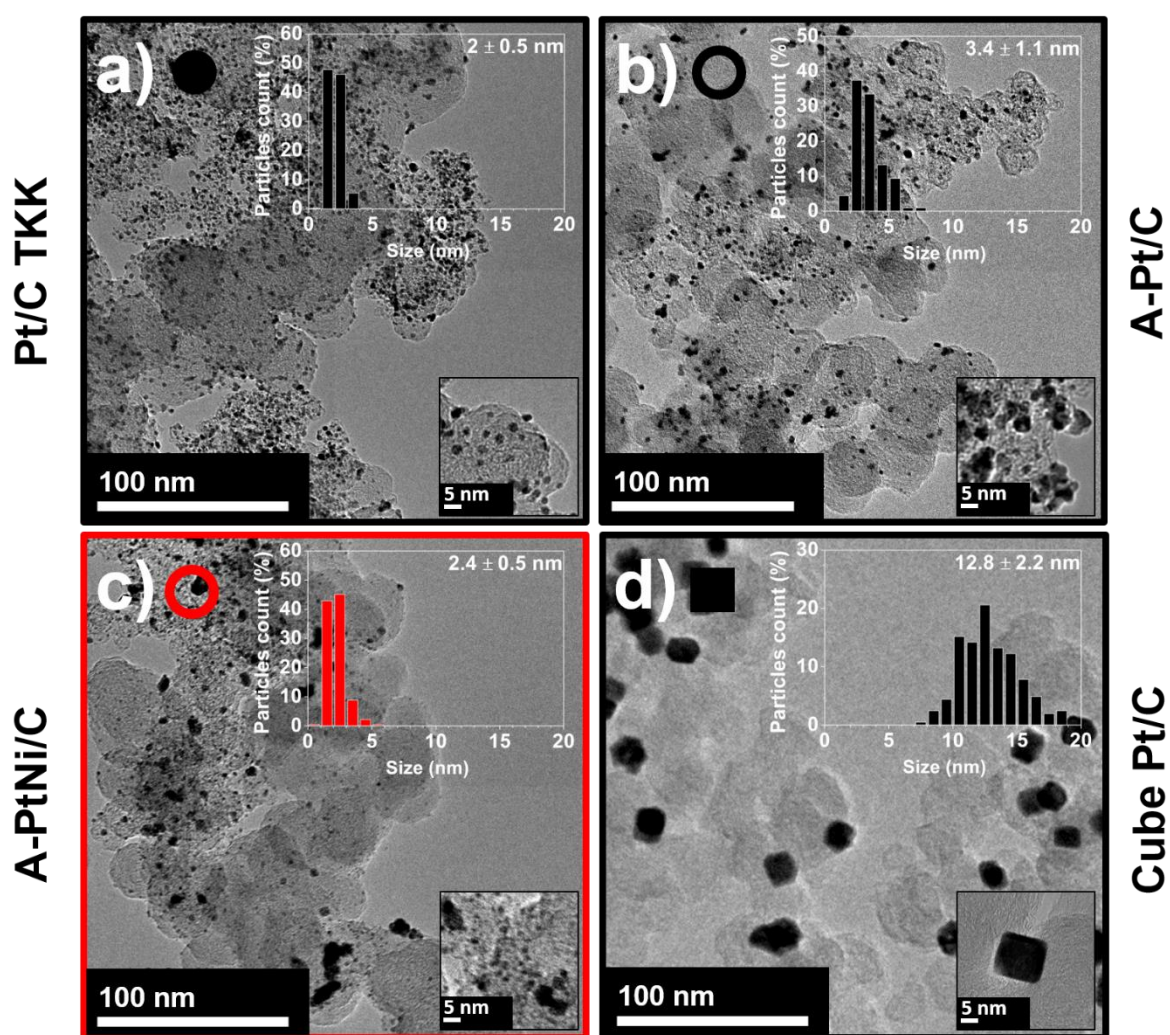
$$\alpha_3 = -2.2 * 10^{-3} \quad \text{Eq. S15}$$

Finally, the estimation of  $f$  allows the expression of the Surface Distortion descriptor free from the contribution of Ni atoms (‘chemical disorder’) for all the electrocatalysts:

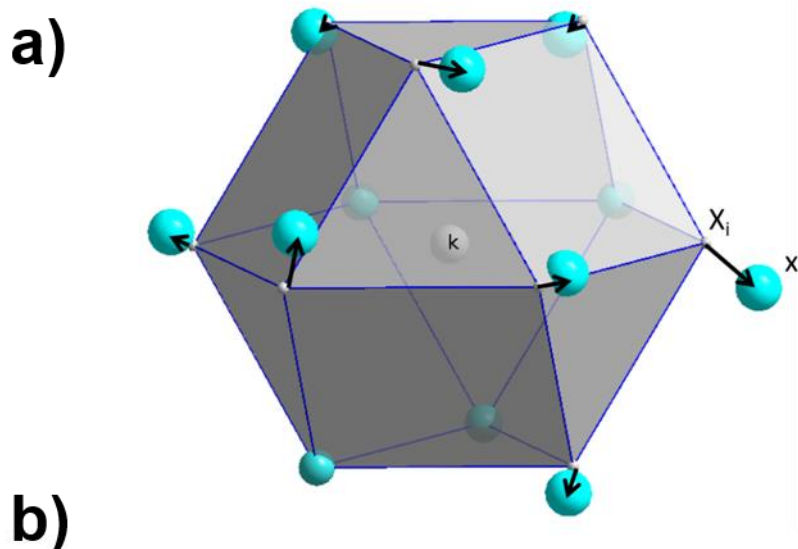
$$SD = \frac{\text{Microstrain} - f(\%Ni)}{D} = CM - \frac{f(Ni)}{D} \quad \text{Eq. S16}$$

Where CM is the corrected microstrain introduced in a previous study<sup>23</sup>. **Eq. S16** shows that SD and CM values are equivalent in case of Ni-poor and small nanocrystallites (which was the case in the mentioned study). The values of SD are displayed in **Table S2**.



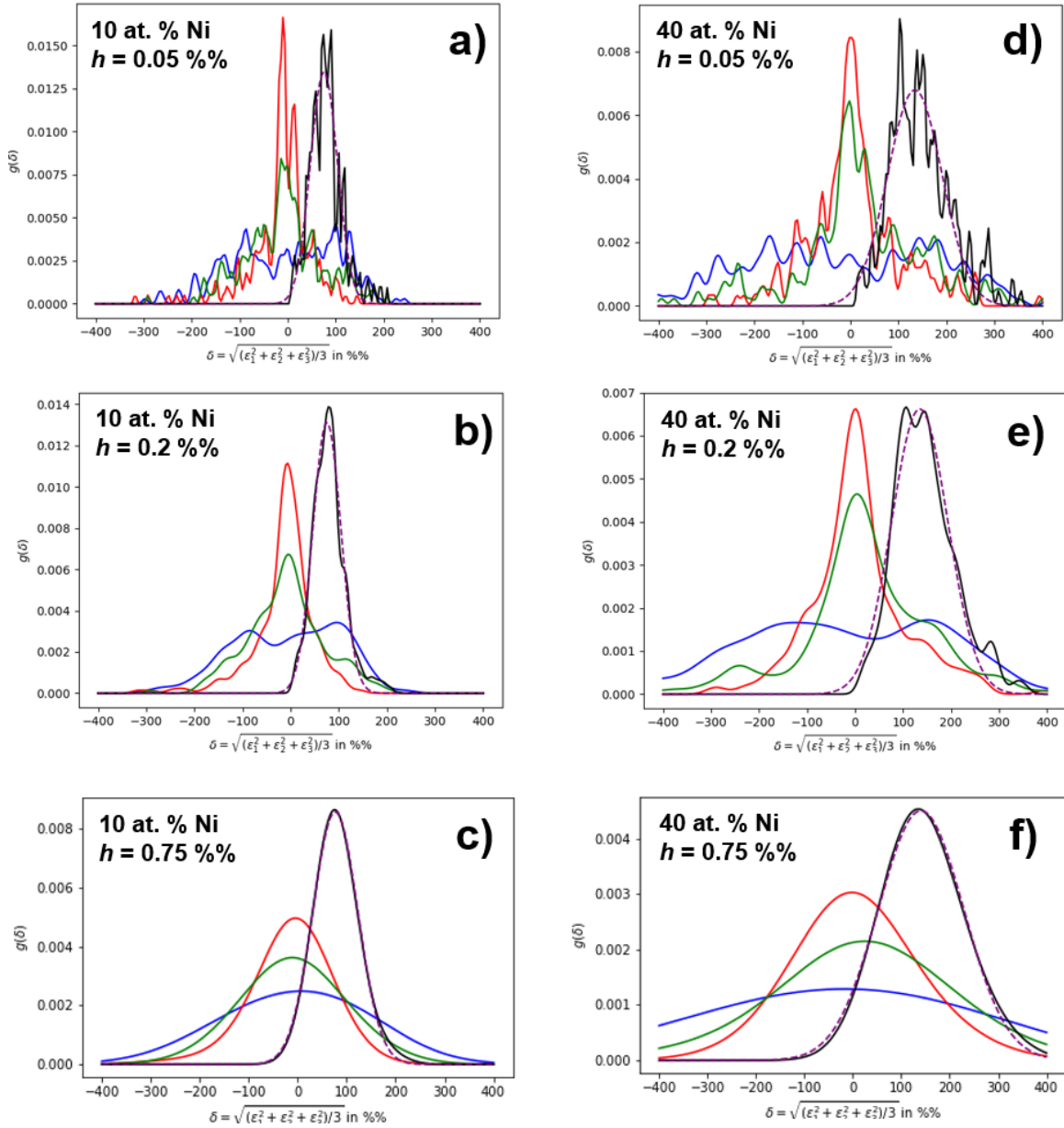


**Supplementary Figure S1. TEM images and particle size distributions of the reference catalysts of this study.** TEM images and particle size distribution of a) Pt/C TKK, b) A-Pt/C (agglomerated Pt/C), c) A-PtNi/C (agglomerated PtNi/C) and d) Cube Pt/C.

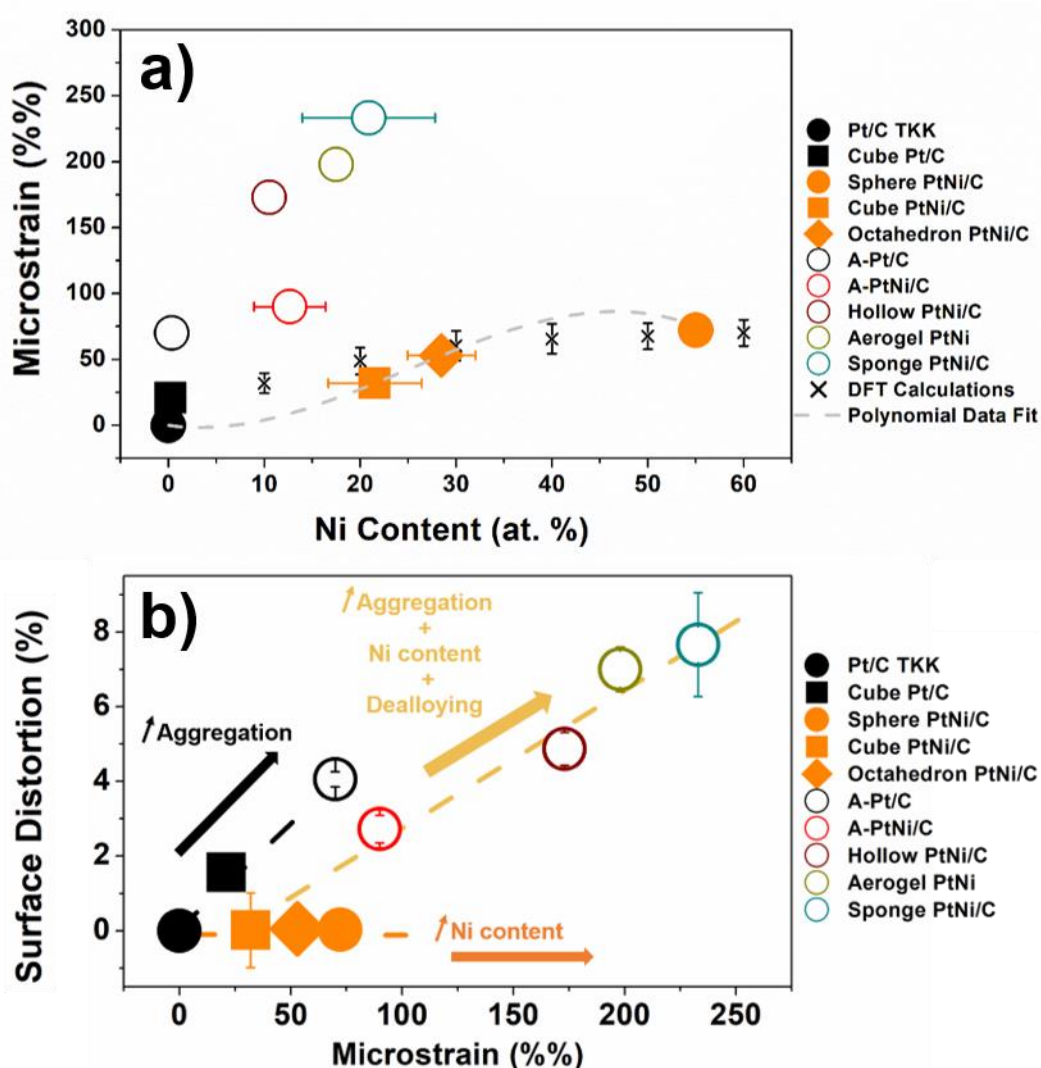


**Supplementary Figure S2. Theoretical approach used to estimate the chemically-induced microstrain in DFT calculations.** a) Schematics and b) results of the calculations. Randomly distributed Ni atoms create local distortions inside the cubic cell. In a perfect bulk fcc structure, the cage made by the 12 neighbouring atoms (materialized in grey) around a central atom (here, labelled  $k$ ) is a perfect cuboctahedron. Upon alloying, displacements of the first neighbours are noticed with respect to these reference locations (black arrows), and an atomic deformation around the central atom may be defined by comparing the deviations between the perfect atomic locations of the neighbours,  $X_i$  and the atomic locations of the neighbours considered in relaxed alloyed structure,  $x_i$  (in blue). The gradient deformation tensor,  $F_k$ , is defined as the 3D operator, which transforms the  $X_i$  into the  $x_i$ . Its components are homogeneous to the space-dependent distortions,  $f_{\alpha\beta} = (\Delta d/d_0)_{\alpha\beta}$ , of the first-neighbour cage, where  $\alpha$  and  $\beta$  indexes run over  $x$ ,  $y$  and  $z$  space variables. The plot in b) shows a bell-shaped curve with a maximum between 40 and 60 at. % Ni. The absolute

values of microstrain and the overall trends are similar whatever the value of the smoothing parameter ( $h$ ) chosen.

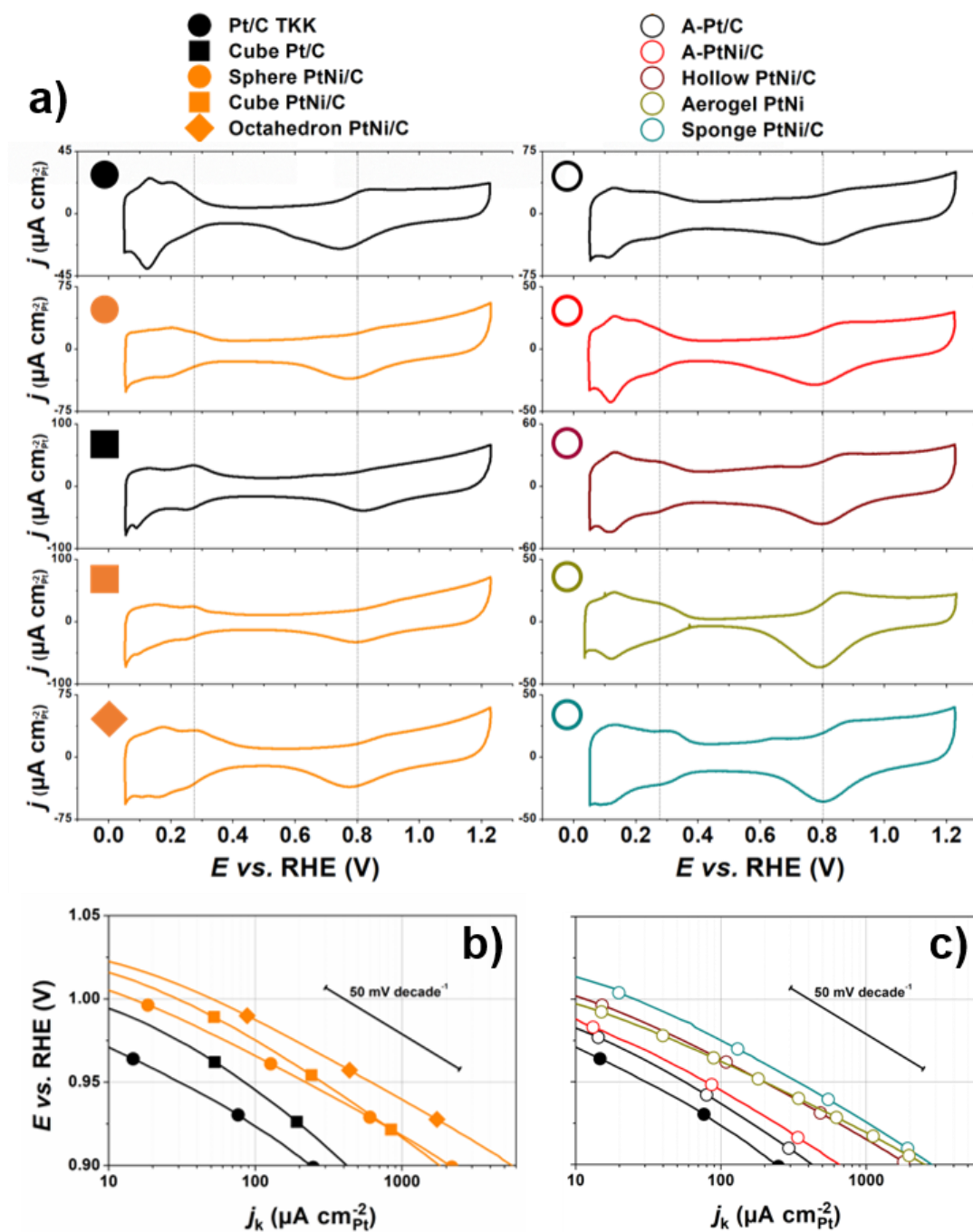


**Supplementary Figure S3. Examples of calculated atomic distortion density distributions.** The distributions are given (black curve) for a 10 at. % Ni cell, obtained with a smoothing parameter  $h$  of a) 0.05 %%, b) 0.2 %% and c) 0.75 %% and for a 40 at. % Ni cell, obtained with a smoothing parameter  $h$  of d) 0.05 %%, e) 0.2 %% and f) 0.75 %%. The distribution functions in  $\epsilon_1$ ,  $\epsilon_2$ , and  $\epsilon_3$  are represented in blue, red and green colours, respectively. The distribution functions are approximated by a Gaussian function represented with dotted purple lines.

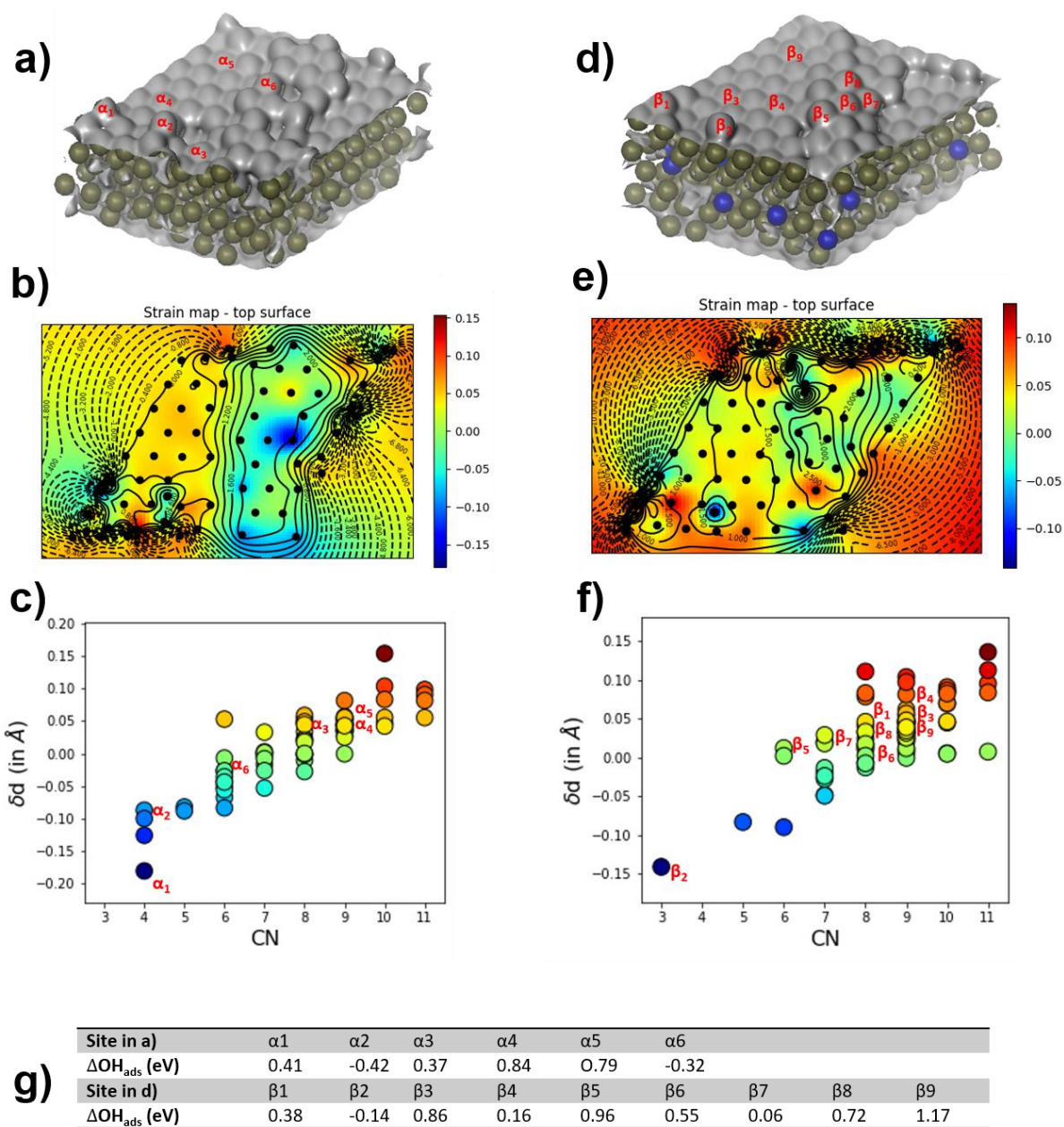


**Supplementary Figure S4. Effect of the Ni at. % on the value of microstrain and Surface Distortion.** The plot in a) shows the microstrain-Ni content relationships for all the electrocatalysts evaluated in this study and DFT calculations data points (estimated for 0, 10, 20, 30, 40, 50, and 60 Ni at. %, black crosses). DFT calculations confirm that the Ni content is a source of microstrain and that the supposed ‘structurally-ordered’ catalysts do not present any significant other contribution to the microstrain (i.e. aggregation or dealloying). For this reason, a polynomial fit of these ‘structurally-ordered’ catalysts (Pt/C TKK, Cube PtNi/C, Octahedron PtNi/C and Sphere PtNi/C) experimental data points was adopted to describe the contribution of the Ni content to the microstrain. In b), the Surface Distortion values plotted as a function of the measured microstrain show that, depending on the catalyst morphology (Ni content, agglomeration, dealloyed surface etc.), the measured microstrain does not necessarily translate into a greater surface distortion. Aggregation and dealloying produce microstrain related to surface distortion, while an increasing Ni content creates bulk microstrain i.e. not specific to the surface.

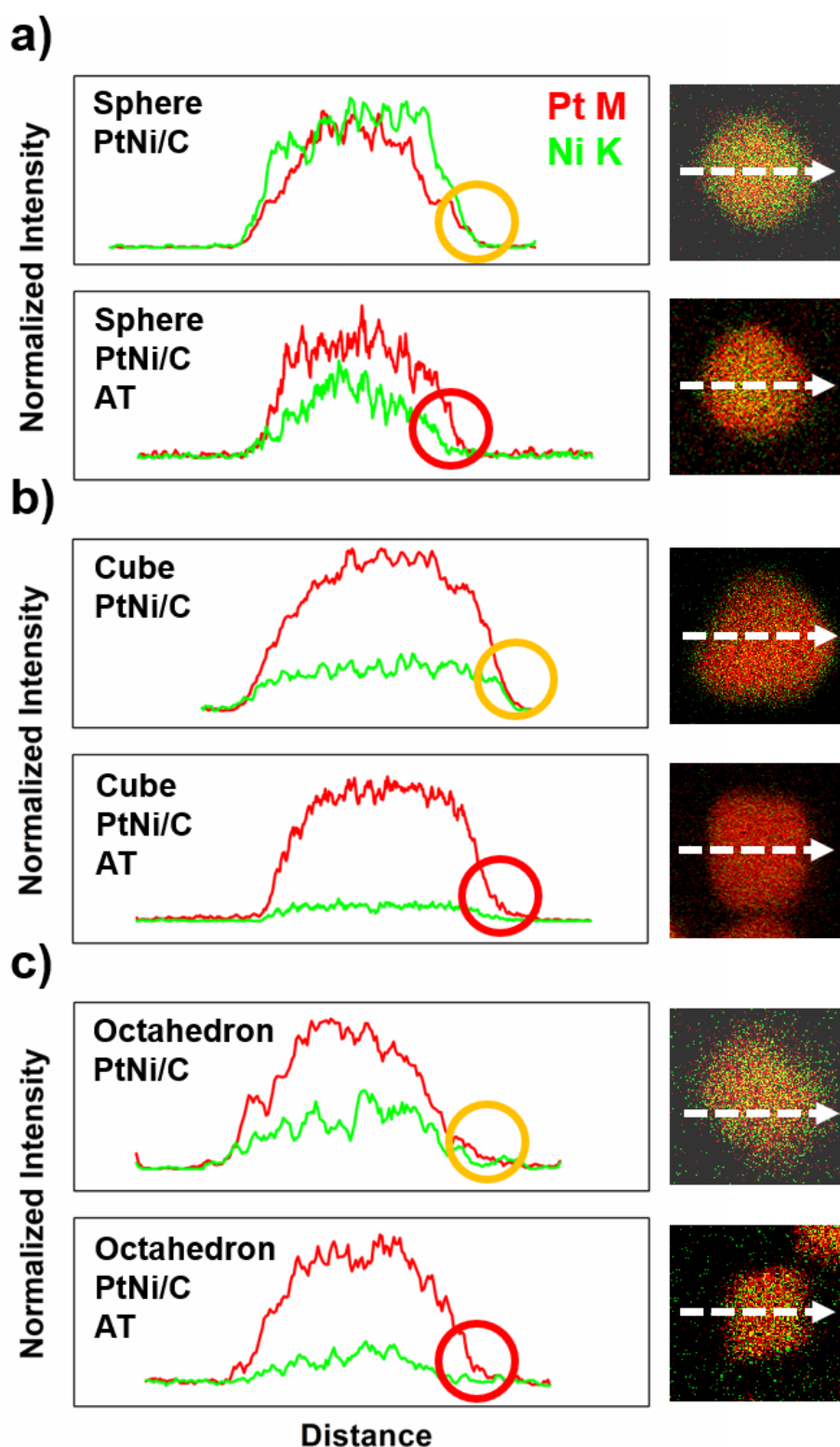




**Supplementary Figure S5. Base voltammograms and Tafel plots of the electrocatalysts evaluated in this study.** The base voltammograms shown in a) were recorded in Ar-saturated 0.1 M HClO<sub>4</sub> at a potential sweep rate of 20 mV s<sup>-1</sup>. The Tafel curves were measured at  $\omega = 1600$  rpm after correction for Ohmic losses and O<sub>2</sub> diffusion in O<sub>2</sub>-saturated 0.1 M HClO<sub>4</sub> at a potential sweep rate of 5 mV s<sup>-1</sup> and shown in b) for the ‘structurally-ordered’ materials and in c) for the ‘structurally-disordered’ materials. Other conditions:  $T = 25$  °C. The voltammograms were normalized using the Pt surface area measured from CO<sub>ads</sub> stripping experiments.

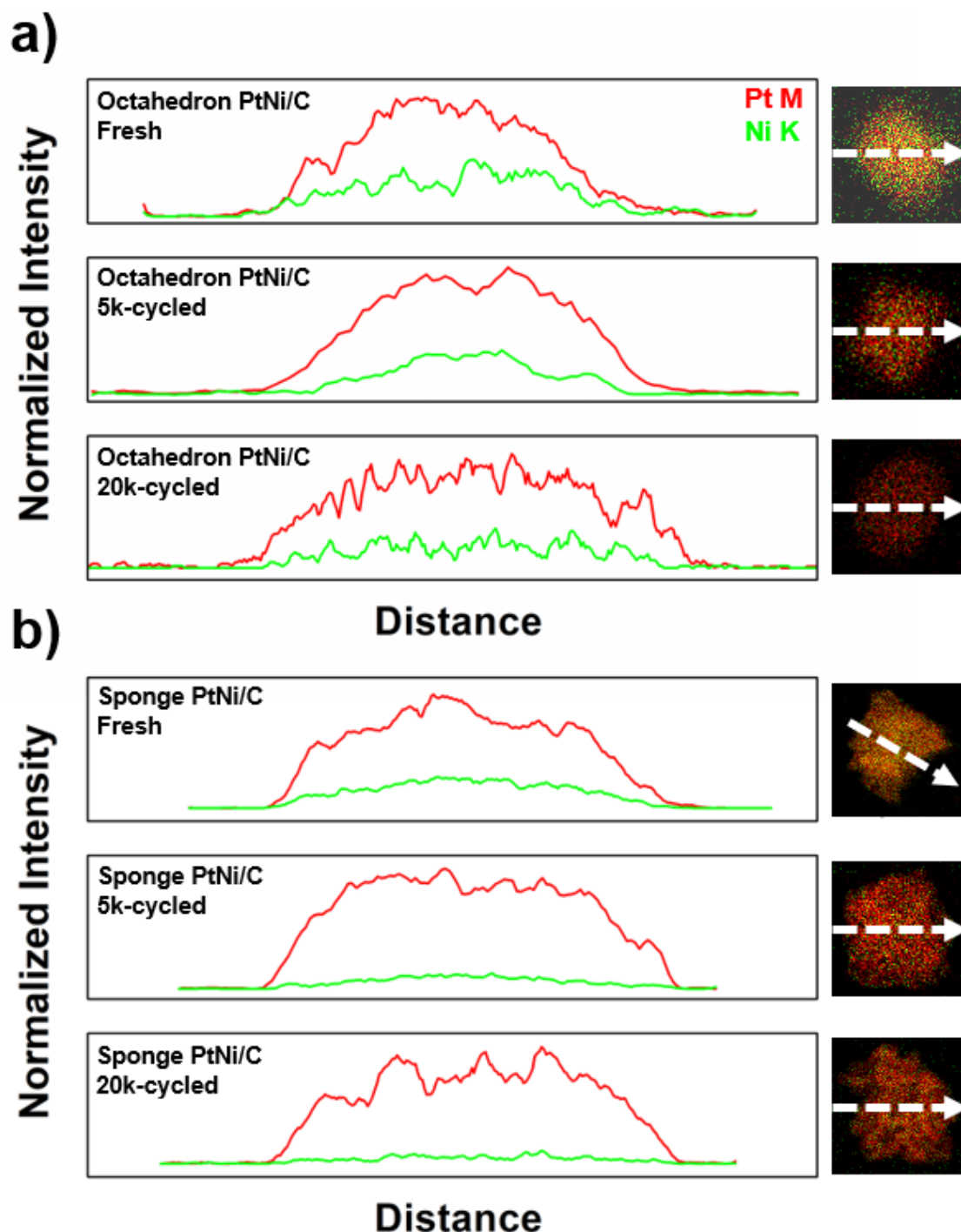


**Supplementary Figure S6. Distortion-coordination number- $OH^*$  binding energy relationships estimated by DFT.** a) Side view after relaxation of the Ni-free 7-layer Pt(111) slab for a density of vacancies ( $\rho_v = 35\%$ ) randomly introduced, b) map of deformation of the surface and d), average deformation centred on each surface site plotted as a function of its CN. The  $OH^*$  adsorption energies relative to Pt(111) shown in g) were have been calculated on catalytic sites labelled in red in a) or c). d), e) and f) correspond to the slab containing residual Ni atoms in its core.



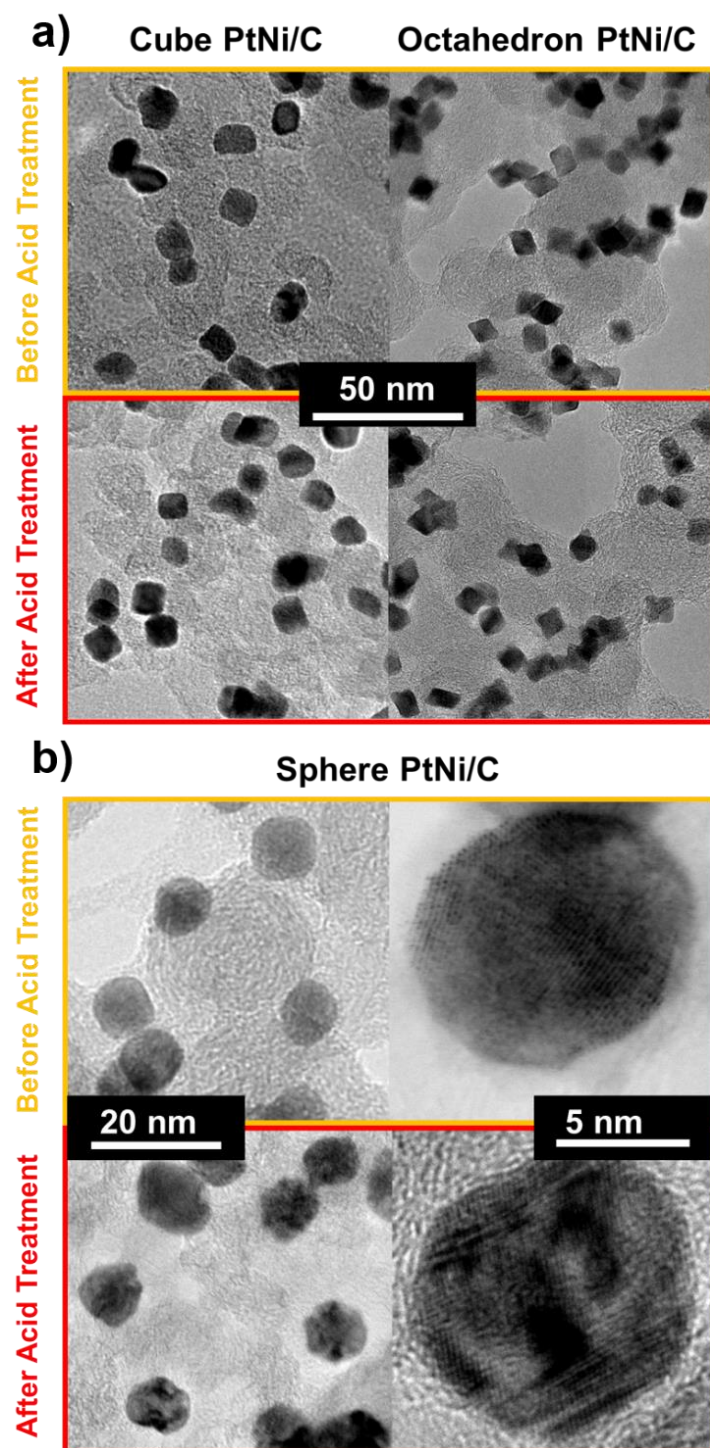
*Supplementary Figure S7. STEM-X-EDS compositional line profiles and elemental maps of the ‘structurally-ordered’ samples before and after acidic treatment in 1.0 M H<sub>2</sub>SO<sub>4</sub> for 22 hours. a) Sphere PtNi/C, b) Cube PtNi/C and c) Octahedron PtNi/C. The STEM-X-EDS profiles are normalized to the elemental scattering factors, allowing a direct reading of the thickness-projected chemical composition*

through the intensity ratios. The circles highlight the surface Pt:Ni stoichiometry changes during the acidic treatments.

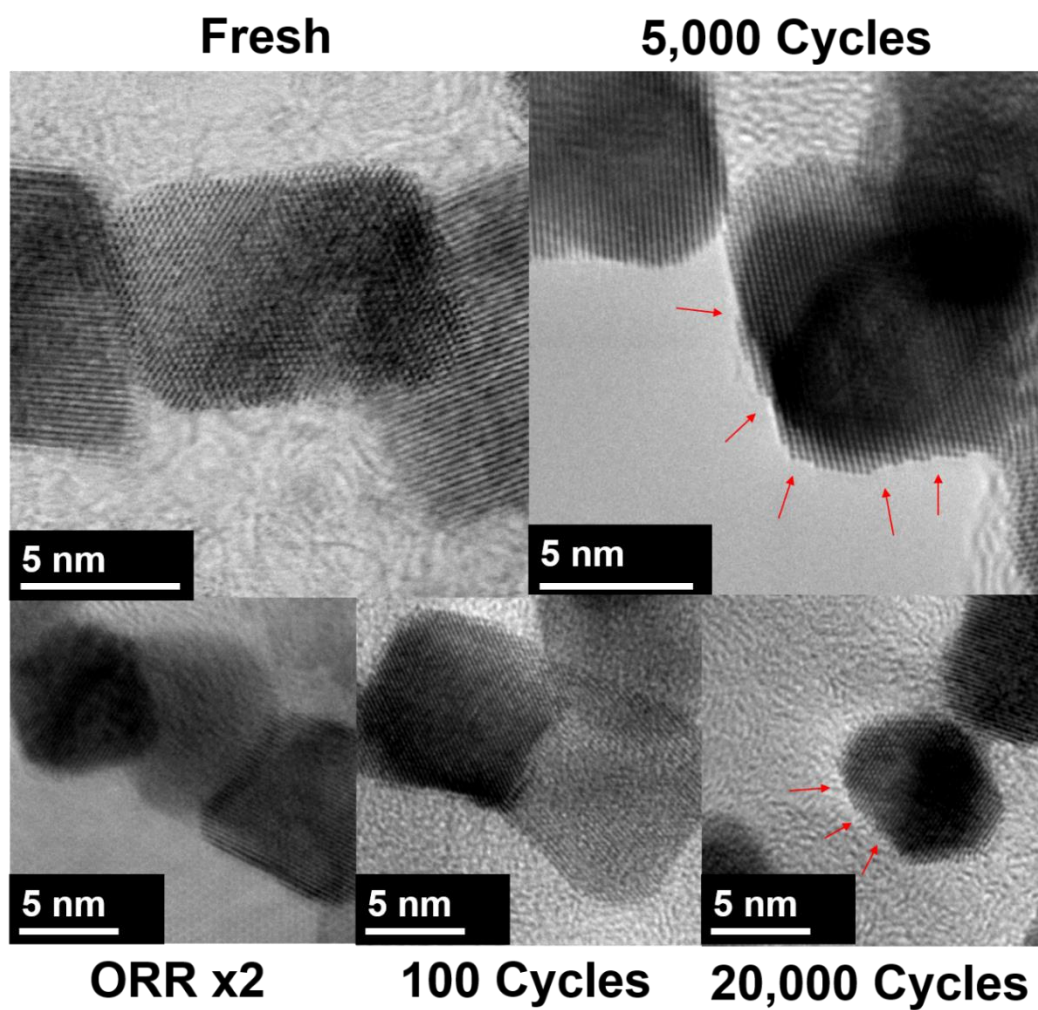


*Supplementary Figure S8. STEM-X-EDS compositional line profiles and elemental maps of the electrochemically aged samples before and after 5,000 and 20,000 potential cycles. a) Octahedron PtNi/C and b) Sponge PtNi/C. The STEM-X-EDS profiles are normalized to the elemental scattering factors, allowing a direct reading of the thickness-projected chemical composition through the intensity ratios.*

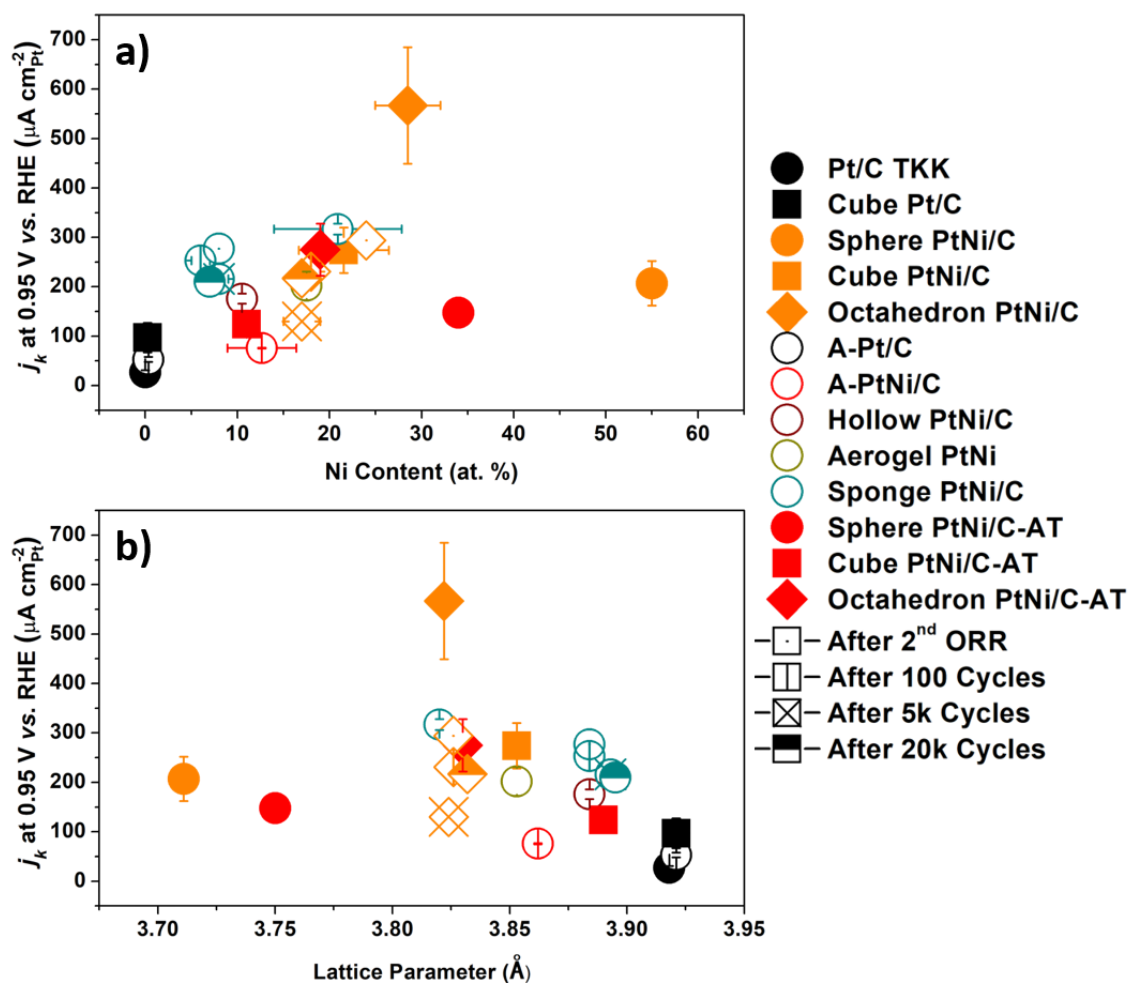




**Supplementary Figure S9.** TEM images of the structurally-ordered nanoparticles (*Cube PtNi/C*, *Sphere PtNi/C* and *Octahedron PtNi/C*) before and after acidic treatment. The pictures in a) show slight emergence of surface convexity and concavity but overall conservation of the particle shape for Cube and Octahedron PtNi/C. The images in b) show the massive advent of porosity after acidic treatment.



*Supplementary Figure S10. HRTEM images of Octahedron PtNi/C after increasing numbers of potential cycles between 0.6 and 1.0 V vs. RHE. The images show the progressive distortion of the surface, especially after 5,000 potential cycles, as highlighted by the red arrows.*



**Supplementary Figure S11. ORR specific activity versus chemical and structural parameters for the fresh and aged materials evaluated in this study. The ORR specific activity shows no direct correlation when plotted neither versus a), the average Ni content nor b) the lattice parameter.**

**Supplementary Table S1. Structural and compositional parameters for the electrocatalysts evaluated in this study.** The Ni content within each catalyst was determined via STEM/X-EDS and Rietveld refinement of the WAXS patterns (i.e. from the lattice parameter using the Vegard's law). Rietveld Refinement was also used to deconvolute the effects of instrumental error, the crystallite size and the microstrain on the broadening of WAXS patterns.

Electrocatalysts	X-EDS	Synchrotron WAXS + Rietveld Refinement				Average Ni content (at. %)
	Ni content (at. %)	Ni content (at. %)	Lattice parameter (Å)	Crystallite size (nm)	Microstrain (%%)	
Sphere PtNi/C	56 ± 1	56	3.711	8.6 ± 0.4	72	56 ± 1
Cube PtNi/C	25 ± 2	18	3.853	12.9 ± 0.6	32	22 ± 5
Octahedron PtNi/C	31 ± 1	26	3.822	9.2 ± 0.3	53	29 ± 3
Hollow PtNi/C	11 ± 3	10	3.884	3.3 ± 0.5	173	11 ± 1
Aerogel PtNi	17 ± 2	18	3.853	4.8 ± 0.6	198	18 ± 1
Sponge PtNi/C	16 ± 1	26	3.820	4.5 ± 0.9	233	21 ± 5
Pt/C TKK	0	0	3.918	1.3 ± 0.2	0	0
A-Pt/C	0	0	3.921	7.4 ± 0.6	70	0
A-PtNi/C	10 ± 4	15	3.862	4 ± 0.5	90	13 ± 5
Cube Pt/C	0	0	3.921	9.5 ± 0.2	21	0

**Supplementary Table S2. Structural parameters derived from the Rietveld analysis of the WAXS patterns for the PtNi/C electrocatalysts evaluated in this study.** The D values were determined using the average crystallite size and SD calculated from the values of D, microstrain and Ni content (see Eqs. S5-S16).

Electrocatalysts	D (%)	SD (%)
Sphere PtNi/C	7.4 ± 2	0.1 ± 0.1
Cube PtNi/C	10.4 ± 0.6	0.0 ± 1.0
Octahedron PtNi/C	14.1 ± 0.6	0.0 ± 0.5
Hollow PtNi/C	35.0 ± 6	4.8 ± 0.4
Aerogel PtNi	25.7 ± 4	7.0 ± 0.6
Sponge PtNi/C	28 ± 6.0	7.6 ± 1.4
Pt/C TKK	65 ± 8	0.0
A-Pt/C	17.4 ± 2	4.0 ± 0.2
A-PtNi/C	30 ± 4	2.7 ± 0.4
Cube Pt/C	13.5 ± 0.6	1.6 ± 0.1

**Supplementary Table S3. Pt specific surface area ( $S_{\text{Pt,CO}}$ ),  $iR$  + mass transport corrected ORR specific activity ( $SA_{0.95}$ ) and mass activity ( $MA_{0.95}$ ) measured at  $E = 0.95$  V vs. RHE on the electrocatalysts used in this study, and corresponding enhancement factors (E.F.) compared to the reference Pt/C TKK.**

Electrocatalysts	$S_{\text{Pt,CO}}$ ( $\text{m}^2 \text{g}_{\text{Pt}}^{-1}$ )	$SA_{0.95}$ ( $\mu\text{A cm}_{\text{Pt}}^{-2}$ )	E.F. SA	$MA_{0.95}$ ( $\text{A g}_{\text{Pt}}^{-1}$ )	E.F. MA
Sphere PtNi/C	$47 \pm 1$	$207 \pm 45$	7.7	$97 \pm 2$	4.6
Cube PtNi/C	$24 \pm 2$	$274 \pm 46$	10.1	$67 \pm 5$	3.2
Octahedron PtNi/C	$28 \pm 3$	$567 \pm 118$	21	$157 \pm 19$	7.5
Hollow PtNi/C	$45 \pm 7$	$176 \pm 10$	6.5	$79 \pm 12$	3.7
Aerogel PtNi	$31 \pm 2$	$202 \pm 29$	7.5	$62 \pm 5$	3
Sponge PtNi/C	$46 \pm 2$	$317 \pm 11$	11.7	$146 \pm 4$	6.9
Pt/C TKK	$78 \pm 5$	$27 \pm 4$	1.0	$21 \pm 1$	1.0
A-Pt/C	$36 \pm 1$	$53 \pm 5$	2.0	19	0.9
A-PtNi/C	$39 \pm 1$	$76 \pm 1$	2.8	$30 \pm 1$	1.4
Cube Pt/C	$12 \pm 1$	$97 \pm 30$	3.6	$11 \pm 1$	0.5

**Supplementary Table S4. Structural and chemical parameters for the aged PtNi/C electrocatalysts.**

Electrocatalysts	X-EDS	Synchrotron WAXS + Rietveld Refinement				Average Ni content (at. %)
	Ni content (at. %)	Ni content (at. %)	Lattice parameter (Å)	Crystallite size (nm)	Microstrain (%%)	
Sphere PtNi/C-AT	$34 \pm 1$	44	3.750	$11.6 \pm 1.8$	130	$39.0 \pm 6$
Cube PtNi/C-AT	$11 \pm 1$	9	3.890	$10.1 \pm 0.2$	14	$10.0 \pm 2$
Octahedron PtNi/C-AT	$19 \pm 1$	25	3.830	$8.3 \pm 0.4$	45	$22.0 \pm 4$
Octahedron PtNi/C-2 <sup>nd</sup> ORR	$24 \pm 1$	25	3.826	7.1	20	$24.5 \pm 2$
Octahedron PtNi/C-100	$18 \pm 1$	25	3.826	7.7	21	$21.5 \pm 5$
Octahedron PtNi/C-5k	$17 \pm 2$	25	3.824	9.4	51	$21.0 \pm 6$
Octahedron PtNi/C-20k	$17 \pm 1$	23	3.832	9.5	52	$20.0 \pm 4$
Sponge PtNi/C-2 <sup>nd</sup> ORR	$8 \pm 1$	10	3.884	8.5	79	$9.0 \pm 2$
Sponge PtNi/C-100	$6 \pm 1$	10	3.884	8.3	68	$8.0 \pm 3$
Sponge PtNi/C-5k	$8 \pm 1$	8	3.893	6.9	70	$8.0 \pm 1$
Sponge PtNi/C-20k	$7 \pm 1$	7	3.895	7.3	58	$7.0 \pm 1$

**Supplementary Table S5. Structural parameters derived from the Rietveld analysis of the WAXS patterns for the aged PtNi/C electrocatalysts.**

Electrocatalysts	$D$ (%)	$SD$ (%)
Sphere PtNi/C-AT	$12 \pm 2$	$5.1 \pm 1$
Cube PtNi/C-AT	$13 \pm 0.3$	$0.8 \pm 0.2$
Octahedron PtNi/C-AT	$16 \pm 1$	$0.8 \pm 0.6$
Octahedron PtNi/C-2 <sup>nd</sup> ORR	$18 \pm 1$	$15.6 \pm 1$
Octahedron PtNi/C-100	$17 \pm 2$	$-1.2 \pm 0.1$
Octahedron PtNi/C-5k	$14 \pm 1$	$1.5 \pm 1$
Octahedron PtNi/C-20k	$14 \pm 1$	$1.7 \pm 1$
Sponge PtNi/C-2 <sup>nd</sup> ORR	$16 \pm 3$	$5.1 \pm 1$
Sponge PtNi/C-100	$16 \pm 2$	$4.2 \pm 1$
Sponge PtNi/C-5k	$19 \pm 3$	$3.6 \pm 1$
Sponge PtNi/C-20k	$17 \pm 2$	$3.3 \pm 1$

**Supplementary Table S6. *iR* + mass transport corrected ORR specific activity ( $SA_{0.95}$ ) and mass activity ( $MA_{0.95}$ ) measured at  $E = 0.95$  V vs. RHE for the aged PtNi/C electrocatalysts. The  $MA_{0.95}$  values were calculated by normalizing the kinetic current for the ORR by the Pt mass initially loaded on the electrode.**

Catalysts	$SA_{0.95}$ ( $\mu\text{A cm}_{\text{Pt}}^{-2}$ )	$MA_{0.95}$ ( $\text{A g}_{\text{Pt}}^{-1}$ )
Octahedron PtNi/C	$567 \pm 118$	$157 \pm 19$
Octahedron PtNi/C-2 <sup>nd</sup> ORR	294	81
Octahedron PtNi/C-100	231	64
Octahedron PtNi/C-5k	130	36
Octahedron PtNi/C-20k	217	60
Sponge PtNi/C	$317 \pm 11$	$146 \pm 4$
Sponge PtNi/C-2 <sup>nd</sup> ORR	277	127
Sponge PtNi/C-100	253	116
Sponge PtNi/C-5k	216	100
Sponge PtNi/C-20k	210	97

## References

- Oh, H. S., Oh, J. G., Hong, Y. G. & Kim, H. Investigation of carbon-supported Pt nanocatalyst preparation by the polyol process for fuel cell applications. *Electrochim. Acta* **52**, 7278–7285 (2007).
- Henning, S. *et al.* Pt-Ni aerogels as unsupported electrocatalysts for the oxygen reduction reaction. *J. Electrochem. Soc.* **163**, F998–F1003 (2016).
- Zhang, J., Yang, H., Fang, J. & Zou, S. Synthesis and oxygen reduction activity of shape-controlled Pt<sub>3</sub>Ni nanopolyhedra. *Nano Lett.* **10**, 638–644 (2010).
- Gan, L., Rudi, S., Cui, C., Heggen, M. & Strasser, P. Size-controlled synthesis of sub-10 nm PtNi<sub>3</sub> alloy nanoparticles and their unusual Volcano-shaped size effect on ORR electrocatalysis. *Small* **12**, 3189–3196 (2016).
- Ashiotis, G. *et al.* The fast azimuthal integration Python library: PyFAI. *J. Appl. Crystallogr.* **48**, 510–519 (2015).
- Rodríguez-Carvajal, J. Recent advances in magnetic structure determination by neutron powder diffraction. *Phys. B Condens. Matter* **192**, 55–69 (1993).
- Thompson, P., Cox, D. E. & Hastings, J. B. Rietveld refinement of Debye-Scherrer synchrotron X-ray data from Al<sub>2</sub>O<sub>3</sub>. *J. Appl. Crystallogr.* **20**, 79–83 (1987).
- Parzen, E. On estimation of a probability density function and mode. *Ann. Math. Stat.* **33**, 1065–1076 (1962).
- Kresse, G. & Furthmüller, J. Efficiency of ab-initio total energy calculations for metals and semiconductors using a plane-wave basis set. *Comput. Mater. Sci.* **6**, 15–50 (1996).
- Joubert, D. From ultrasoft pseudopotentials to the projector augmented-wave method. *Phys. Rev. B - Condens. Matter Mater. Phys.* **59**, 1758–1775 (1999).
- Perdew, J. P., Burke, K., Ernzerhof, M. & Ernzerhof, M. Generalized gradient approximation made simple. *Phys. Rev. Lett.* **77**, 3865 (1996).

12. *Hans Hellmann: Einführung in die Quantenchemie.* (Dirk Andrae, 1937).
13. Feynman, R. P. Forces in molecules. *Phys. Rev.* **56**, 340–343 (1939).
14. Methfessel, M. & Paxton, A. T. High-precision sampling for Brillouin-zone integration in metals. *Phys. Rev. B* **40**, 3616–3621 (1989).
15. Stukowski, A., Markmann, J., Weissmüller, J. & Albe, K. Atomistic origin of microstrain broadening in diffraction data of nanocrystalline solids. *Acta Mater.* **57**, 1648–1654 (2009).
16. Le Bacq, O. *et al.* Effect of atomic vacancies on the structure and the electrocatalytic activity of Pt-rich/C nanoparticles: A combined experimental and density functional theory study. *ChemCatChem* **9**, 2324–2338 (2017).
17. Nørskov, J. K. *et al.* Origin of the overpotential for oxygen reduction at a fuel-cell cathode. *J. Phys. Chem. B* **108**, 17886–17892 (2004).
18. Stephens, I. E. L., Bondarenko, A. S., Grønbjerg, U., Rossmeisl, J. & Chorkendorff, I. Understanding the electrocatalysis of oxygen reduction on platinum and its alloys. *Energy Environ. Sci.* **5**, 6744 (2012).
19. Schmidt, T. J. *et al.* Characterization of high-surface-area electrocatalysts using a rotating disk electrode configuration. *J. Electrochem. Soc.* **145**, 2354 (1998).
20. Garsany, Y., Singer, I. L. & Swider-Lyons, K. E. Impact of film drying procedures on RDE characterization of Pt/VC electrocatalysts. *J. Electroanal. Chem.* **662**, 396–406 (2011).
21. Montejano-Carrizales, J. M. & Morán-López, J. L. Geometrical characteristics of compact nanoclusters. *Nanostructured Mater.* **1**, 397–409 (1992).
22. Montejano-Carrizales, J. M., Aguilera-Granja, F. & Morán-López, J. L. Direct enumeration of the geometrical characteristics of clusters. *Nanostructured Mater.* **8**, 269–287 (1997).
23. Chattot, R. *et al.* Beyond strain and ligand effects: Microstrain-induced enhancement of the oxygen reduction reaction kinetics on various PtNi/C nanostructures. *ACS Catal.* **7**, 398–408 (2017).